RSC Advances

ROYAL SOCIETY OF CHEMISTRY

www.rsc.org/advances

Journal Name

COMMUNICATION

A "Pillared" Process to Construct Graphitic Carbon Nitride Based Functionalized Mesoporous Materials

Received 00th January 20xx,
Accepted 00th January 20xx

DOI: 10.1039/x0xx00000x

www.rsc.org/

Zhonghao Wang,[ab] Long Chen,[a] Xiaorui Du,[a] Guojun Zou*[a] and Xiaolai Wang*[a]

We present a novel method to prepare mesoporous materials via in situ self-assembly of graphitic carbon nitride nanosheets and silica nanoparticles. Combining the advantages of g-C_3N_4 nanosheets and mesoporous structure, the as-prepared materials exhibit superior adsorption capabilities for heavy metal ions and organic pollutants.

Mesoporous materials have been widely studied in the area of catalysis,[1] energy storage and conversion,[2] adsorption,[3-5] and biomedicine[6, 7] due to their unique features and properties. In general, mesoporous materials are synthesized based on the nanocasting method by employing costly organic molecules as "soft" template[8-12] or by using mesoporous materials as "hard" template.[13] The key drawback of the method is the extra steps required to remove templates, which not only increase the cost but also result in the production of harmful gases due to the removal of the organic templates by combustion at high temperature. Therefore, a modified procedure for the synthesis of porous materials without using templates is of particular interest. Recently, Yan's group proposed a novel method to prepare three-dimensional (3D) graphene/ nanoparticle composites without any templates,[14] and Gao's group obtained 3D graphene/carbon nanotubes composites via a simple cryodesiccation procedure.[15] These work represent an important step toward green and facile synthesis of composite materials in the future.

Graphitic carbon nitride (g-C_3N_4), a metal-free polymer semiconductor, possesses a graphite-like structure with weak van der Waals forces between C-N layers.[16] Since its discovery, g-C_3N_4 has been studied in many areas such as catalysis,[17, 18] bioimaging,[19-21] and photosynthesis.[22-27] The two-dimensional (2D) g-C_3N_4 nanosheets (CNS), which can be obtained by various methods including thermal oxidation "etching",[28] and liquid phase exfoliation by sonication or strong acid,[19, 23, 29, 30] have exceptional properties with respect to bulk g-C_3N_4. Particularly, the negatively charged CNS may interact efficiently with the nanoparticles (NPs) that are positively charged. Considering the affinity between g-C_3N_4 and graphene, and that the solubility of CNS can be tuned by changing pH value and operation temperature,[30] CNS could be used as 2D nanosheets matrix to assemble NPs, leading to 3D CNS/NPs porous materials.

In this study, we demonstrate a novel approach to fabricate mesoporous materials by employing 2D CNS as matrix to capture SiO_2 NPs in liquid phase. The products obtained after simple processing exhibit high surface areas and uniform pore size distribution. This "pillared" strategy may be applied to fabricate various CNS-based functional materials by replacing SiO_2 NPs with other NPs.

The strategy for synthesis of CNS-based mesoporous materials is illustrated in scheme1. As described in our previous work,[30] bulk g-C_3N_4 was exfoliated to 2D nanosheets and the obtained CNS show pH value-dependent properties. Similar to a process of fishing, the nanoparticles are the "fishes", and the CNS can be viewed as "fishnets". The combination of CNS and NPs tend to form a network by self-assembly when the pH value of the system is altered. In this way, the NPs can be captured into the network of nanosheets in a simple one-step process. In principle, any acid resistant NPs homogeneously dispersed in aqueous solution could be embedded into the CNS network to form g-C_3N_4/NPs composite materials.

The crystal structures of the samples were evaluated using X-ray diffraction. XRD measurements show the diffraction patterns typical for g-C_3N_4 (Figure 1A). The strong reflection at 27.2° for bulk g-C_3N_4 corresponds to the (002) planes, characteristic of interplanar stacking of graphitic materials.[16, 30] In contrast with the bulk g-C_3N_4, a slight shift to 27.8° and a sharp decrease in the overall intensity for the (002) peak can be observed for SiO_2-*x*N/C_3N_4. These are possibly due to the decreased interlayer distance of g-C_3N_4 and the lower contents

[a] State Key Laboratory for Oxo Synthesis and Selective Oxidation, Lanzhou Institute of Chemical Physics, Chinese Academy of Sciences, Lanzhou, 730000, China. E-Mail: zougj@licp.cas.cn, xlwang@licp.cas.cn
[b] University of Chinese Academy of Sciences, Beijing, 100049, China.
Electronic Supplementary Information (ESI) available: [details of any supplementary information available should be included here]. See DOI: 10.1039/x0xx00000x

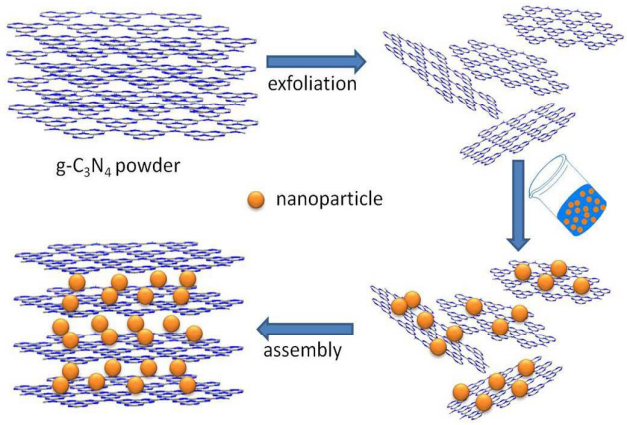

Scheme 1. Schematic illustration for the preparation of SiO_2/CNS nano-composites.

of g-C_3N_4 in SiO_2-*x*N/g-C_3N_4 as compared to the bulk sample. Furthermore, the additional peak, which is assigned to an in-plane structure packing of bulk g-C_3N_4 (13˚), shifts negatively (12˚) and becomes broadened with increasing SiO_2 contents. During the process of exfoliating bulk g-C_3N_4 into CNS, the crystal structure of the nanosheets substantially remains the same except that the reflection peak becomes less pronounced.[29] While after activation by protonation, the peak at 27.4˚ (bulk-g-C_3N_4) which reflects the characteristic interlayer-stacking of aromatic system shifts to a higher angle.[30] The results of XRD patterns are similar to the results that caused by protonation (Figure S1). However, the preparation process of the materials here was performed under alkaline condition, and the shifts of XRD peaks should not be attributed to protonation. Furthermore, the protonated g-C_3N_4 can be recovered by calcinations, while the samples in this work are not. Thus, the shift of the peaks could be ascribed to the pillared effect, which was induced by the external stress caused by SiO_2 nanoparticles and decreased the slight undulation of the CNS. The stretched properties of g-C_3N_4 induced by external stress defined as "flatting effect" (Figure S2). Moreover, the amorphous SiO_2 peak at about 22˚ becomes more obvious as the SiO_2 contents increase. These observations confirm that the structures of g-C_3N_4 and SiO_2 NPs were preserved in the samples.

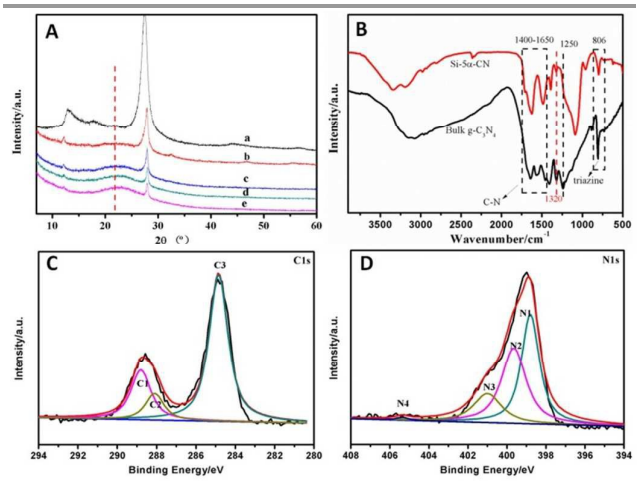

Figure 1. XRD patterns (A) of bulk g-C_3N_4 (a), SiO_2-*x*α-g-C_3N_4 composites (b: *x*=2, c: *x*=5, d: *x*=8, e: *x*=11). FT-IR spectra (B) and XPS profile of N1s(C), C1s (D) of Si-5α-CN sample.

The structures and compositions of the SiO_2-*x*α-g-C_3N_4 were further investigated by Fourier transform infrared spectroscopy (FTIR), X-ray photoelectron spectroscopy (XPS), and Elemental analysis (EA). The strong FTIR absorption bands of Si-5α-CN shown in Figure 1B further reveal the typical molecular structure of g-C_3N_4. The absorption bands in the 1200-1600cm^{-1} region manifest the typical stretching mode of aromatic CN heterocycles. The sharp band at 806cm^{-1} can be attributed to triazine ring mode, which corresponds to condensed CN heterocycles.[23, 30] The broad band at 3000-3500 cm^{-1} may be related to uncondensed terminal amino groups (-NH_2 or =NH groups) and O-H groups from water molecules and SiO_2. In addition, the peak at 1085cm^{-1} is attributed to the asymmetric stretching vibrations of Si-O-Si.[31] Note that the absorption peaks at about 1320 and 1250 cm^{-1} for Si-5α-CN become less pronounced as compared to the bulk sample. The flatting effect of SiO_2 as described in XRD analysis will reduce the asymmetry of the N-$(C)_3$ group, leading to the weakened absorption intensity. This can be rationalized by the acidification instead of SiO_2 flatting effect as demonstrated in our previous studies.[30] The FTIR results for SiO_2-5α-CN composite are in good agreement with those of bulk g-C_3N_4, implying that the basic unit of g-C_3N_4 was not destroyed.[32-34]

The surface chemical states of Si-5α-CN and the bulk g-C_3N_4 were studied by XPS (Figures 1C-D and Figures S3-S4). As shown in Figure S3, the sample is comprised of C, N, Si and O elements. To gain insight into the chemical bonding between the carbon and nitrogen atoms in the samples, the high resolution C1s was further deconvoluted into three Gaussian-Lorenzian peaks. The peak centered at 288.7eV is assigned to the sp^2 hybridized carbon in the triazine ring bonded to the –NH_2 group, while the peak at 287.9eV is attributed to the sp^2 hybridized carbon bonded to N inside the triazine rings.[35] The peak at 284.6eV is typically ascribed to the signal of standard reference carbon.[30] The high resolution XPS spectrum of N1s could be also fitted with four different peaks. The dominant peak at 398.8eV (denoted as N1 in Figure 1D) is commonly attributed to sp^2 N atoms involved in triazine rings,[35, 37] while N2 peak (at 399.6eV) and N3 peak (at 401eV) are assigned to bridging N atoms in N-$(C)_3$[37] and N atoms bonded with H atoms,[36] respectively. The weak N4 peak (at 405.3eV) can be attributed to the charging effects or positive charge localization in heterocycles and the cyano-group.[32, 37] These assignments are in good agreement with those reported for bulk g-C_3N_4 powder (Figure S4), suggesting that the chemical states and the coordination of carbon and nitrogen in the g-C_3N_4 are retained during the "pillared" process by SiO_2 NPs.

Elemental analysis (EA) was performed to determine the C/N mass ratio in the samples (Table S1). EA of the α sample series give a C/N molar ratio of 0.66, 0.66, 0.74, and 0.77 with

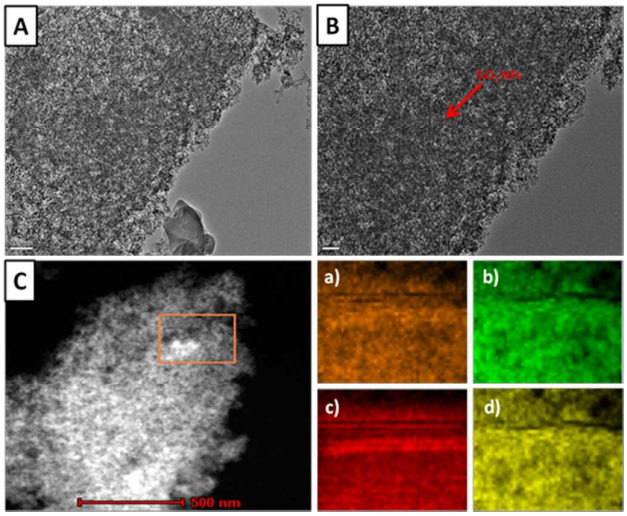

Figure 2. TEM images of Si-5α-CN (A, B). Typical scanning transmission electron microscopy (STEM) image and corresponding elemental mapping images of a) nitrogen, b) silicon, c) carbon, and d) oxygen in the selected area (red rectangle in Figure C).

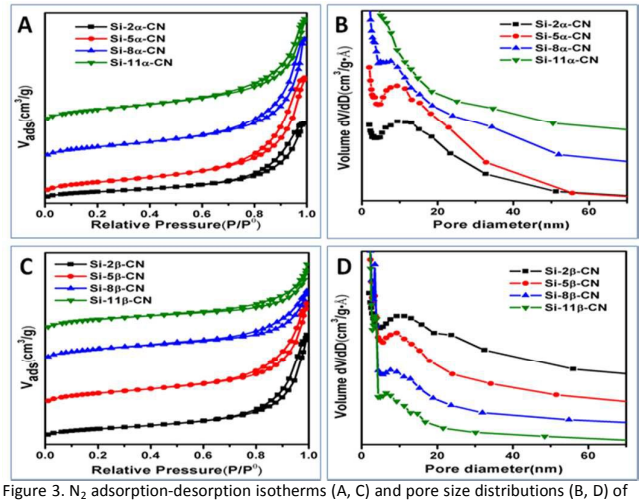

Figure 3. N_2 adsorption-desorption isotherms (A, C) and pore size distributions (B, D) of Si-xN-CN.

increasing SiO_2 contents, indicating excessive amounts of C in Si-8α-CN and Si-11α-CN. This is possibly due to the incomplete hydrolysis of TEOS, leading to the increase of carbon contents with increasing SiO_2 contents. The percentage of g-C_3N_4 in samples changed with the "pillared" SiO_2 contents, and the trend was analyzed and shown in Figure S3. Luckily, a linear relationship between the reciprocal of the percentage content of g-C_3N_4 calculated with EA date and the mass ratio of SiO_2 used in the experiments can be observed. The donated quantities of CNS were consistent during the preparation process of the various mesoporous materials, the reciprocal of the percentage content of g-C_3N_4 is related to the SiO_2 contents of the obtained materials (Figure S5). Hence, the linear relations mentioned above exhibits the direct ratio relationship between SiO_2 NPs used and the SiO_2 contents of the obtained materials, indicating that essentially all of the SiO_2 NPs were wrapped by CNS.

TEM was performed to further investigate the morphology and microstructure of Si-5α-CN. As shown in Figure 2 and Figure S6, the sample with lateral sizes of hundreds of nanometers is observed, which coincides with the CNS without SiO_2 NPs (Figure S4). The nature of the structure can be further unraveled by the element mapping of silicon, carbon, nitrogen, and oxygen in the sample (Figures 2 a), b), c), d)), which indicates a homogeneous dispersion of C, Si, N, and O in Si-5α-CN. Further, the SiO_2 NPs show uniform size distribution, suggesting that the CNS whose solubility changed with the variation of pH value plays a vital role in preventing the agglomeration of SiO_2 NPs during the formation of the mesoporous material.

Combing the results of XRD, XPS, FT-IR and TEM analysis, the typical electronic structure, chemical composition, and tri-s-triazine related bonding of CNS are well established in the obtained materials. Pore structure can be formed when CNS and SiO_2 sol were mixed together, which may impart the materials outstanding physical and chemical properties.

The nitrogen adsorption-desorption isotherms were performed to demonstrate pore structure and pore size distribution of SiO_2-*x*N/g-C_3N_4. Type-IV curves with a H_3 hysteresis loop (Figures 3A and C) are observed supporting that flat type slit pores were formed in all samples. The corresponding pore size distribution curves are shown in Figures 3B and D. The surface areas, pore volumes, and average pore sizes determined from BET isotherms are summarized in Table S2. With the increase of silica contents, the sample surface areas increase significantly. The low surface area observed for the sample with low SiO_2 content could be due to the incompletely pillared effect on CNS. In addition, excessive dosage of silica cannot bring a significant enhancement in surface area and can inhibit the function of g-C_3N_4. Therefore, appropriate g-C_3N_4/SiO_2 ratio is the key to achieving superior "pillared" mesoporous materials. Two types of SiO_2 NPs were synthesized to further reveal the relations between nature of SiO_2 NPs and the properties of the obtained materials (size distribution can be derived from Figure S7). Compared to the α sample series, the β sample series show smaller pore volume. This can be explained by the fact that smaller silica contributed poorly to column brace effect. The pore sizes of α and β mesoporous materials are inclined to diminish and eventually disappeared as the SiO_2 content increased (Figures 3B and D). This may be caused by the fact that excessive flat particles arranged in a more disordered way. So SiO_2-5α-CN was selected as the typical example to perform the following property test. These results indicate that the pore size of the samples can be controlled by the size and contents of the silica used. The as-prepared materials combine the advantages of both CNS and mesoporous properties.

It is important to test its thermal stability for the applications of materials. Temperature programmed heating of Si-5α-CN was carried out and the obtained TG-DSC results are shown in Figure S8. Almost no weight loss appeared below

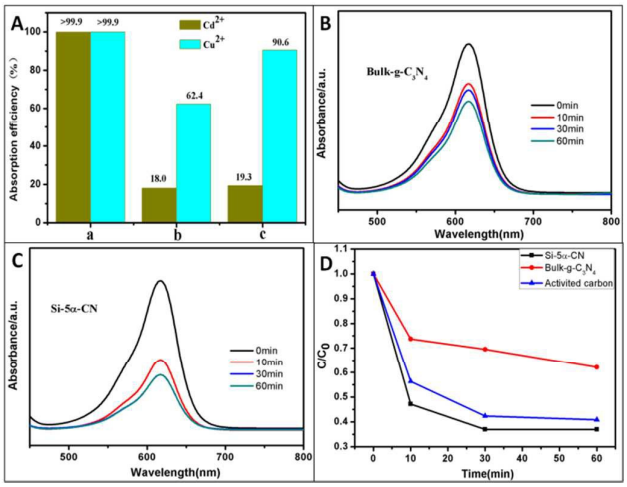

Figure 4. A representatives adsorption efficiency of metal ions of Si-5α-CN (a), bulk-g-C_3N_4 (b), and activated carbon (c). Absorption spectra (B,C) and adsorption rate (D) of an aqueous solution of MG after treatment with adsorbents at different time intervals.

400 ℃ while a 30% weight loss is observed in the temperature ranges from 400 to 630 ℃. It can be concluded that the decomposed of CNS was at the beginning of 400 ℃ compared to the bulk sample at 630 ℃, which may be caused by the "flatting effect" discussed above. The TG results reveal that the materials can be potentially used below 400 ℃.

To evaluate potential application of the as-prepared materials, the adsorption capacities for the heavy metal ions and organic pollutants malachite green (MG) were investigated. The adsorption efficiencies of the SiO_2-5α-CN, commercial activated carbon and bulk g-C_3N_4 for Cu^{2+} and Cd^{2+} were compared under the same operation conditions. As shown in Figure 4A, the adsorption efficiency for Cu^{2+} and Cd^{2+} can reach greater than 99.9% for SiO_2-5α-CN, which means that the contents of metal ions can be lowered down to ppb level. It is obvious that the constructed porous material has better adsorption efficiency for heavy metal ions than bulk g-C_3N_4 and activated carbon. UV-visible (UV-vis) absorption spectroscopy was used to test the adsorption performance for MG (617 nm). Figures 4B, C and S9 show that Si-5α-CN has better adsorption capacity than bulk g-C_3N_4 and activated carbon. Moreover, as shown in Figure 4D, in the first 10 min, a sharp variation in removal ratios can be observed and deemed as a quick adsorption stage. The subsequent second stage between 10 and 30 min displays a smaller removal ratio (10%). Almost no obvious change can be seen after 30 min. The adsorption capability of Si-5α-CN has also been assessed with the cationic dyes methylene blue (MB) (Figure S10). The improved adsorption ability of the as-prepared material can be attributed to the combination of the advantages of g-C_3N_4 and mesoporous structure. In the case of the adsorption of metal ions, the excellent adsorption capacity may be attributed to the strong coordination ability of tri-s-triazine and the uniform nitrogen pore of the sample (Scheme 2). It is reported that g-C_3N_4 exhibits appropriate microstructure, surface terminations with defects, and nitrogen atoms which can be viewed as the active sites for anchoring metal ions.[16, 38] Furthermore, the uniform pore structure and high BET surface area of Si-5α-CN are beneficial for pollutants flowing through the pore and being captured by CNS via coordination. In the case of organic pollutants adsorptions, the high adsorption ability of Si-5α-CN may be largely attributed to the π-π conjugation since g-C_3N_4 nanosheet is similar to graphene (Scheme 2). Overall, the ordered porous structure and high BET surface area of the CNS/SiO_2 composites can facilitate the function of each component. Moreover, SiO_2 NPs may be replaced with other substances such as some biological molecules, quantum dots or TiO_2 NPs to integrate the advantages of both g-C_3N_4 and the "pillared" components, resulting in various novel bifunctional materials.

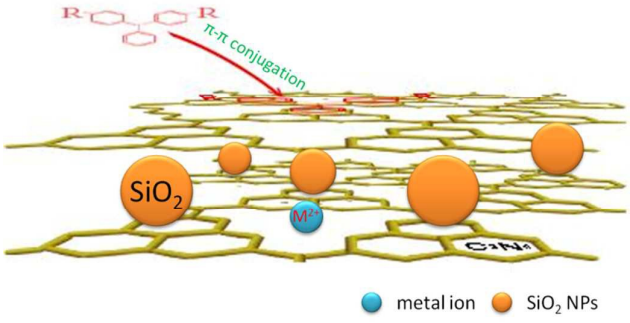

Scheme 2. Adsorption mechanism of SiO_2/CNS for metal ions and organic pollutants.

In summary, by using "pillared" method without any surfactant and hard template, we have successfully fabricated functional mesoporous SiO_2/CNS composites in which the nature of g-C_3N_4 was maintained as compared to bare CNS. The surface areas and pore volumes of the as-prepared materials can be tuned by altering the size and quantity of SiO_2. Combining the advantages of both g-C_3N_4 and ordered porous structures, the prepared SiO_2/CNS composites exhibit excellent performance in removing inorganic or organic pollutants, and can be stabilized up to 400 ℃, which warrant their potential application in energy and environmental fields, such as in catalysis, adsorbent, and so on.

Notes and references

1 A. Corma, *Chem. Rev.*, 1997, **97**, 2373-2420.
2 S. H. Joo, S. J. Choi, I. Oh, J.Kwak, Z. Liu, O. Terasaki and R. Ryoo. *Nature*, 2001, **412**, 169-172.
3 A. Vinu, V. Murugesan, O. Tangermann and M. Hartmann, *Chem. Mater.*, 2004, **16**, 3056-3065.
4 A. M. Liu, K. Hidajat, S. Kawi and D. Y. Zhao, *Chem. Commun.*, 2000, 1145-1146.
5 Z. Sun, Y. Deng, J. Wei, D. Gu, B. Tu and D. Zhao, *Chem. Mater.*, 2011, **23**, 2176-2184.
6 M. Vallet-Regí, L. Ruiz-González, I. Izquierdo-Barba and J. M. González-Calbet, *J. Mater. Chem.*, 2006, **16**, 26-31.
7 J. Liu, C. Li and F. Li, *J. Mater. Chem.*, 2011, **21**, 7175.
8 S. Tanaka, N. Nishiyama, Y. Egashira and K. Ueyama, *Chem. Commun.*, 2005, 2125-2127.
9 C. Liang, K. Hong, G. A. Guiochon, J. W. Mays and S. Dai, *Angew. Chem., Int. Ed.*, 2004, **43**, 5785-5789.

10 Y. Meng, D. Gu, F. Zhang, Y. Shi, H. Yang, Z. Li, C. Yu, B. Tu and D. Zhao, *Angew. Chem.*, *Int. Ed*., 2005, **44**, 7053-7059.
11 F. Zhang, Y. Meng, D. Gu, Y. Yan, C. Yu, B. Tu and D. Zhao, *J. Am. Chem. Soc.*, 2005, **127**, 13508-13509.
12 Y. Meng, D. Gu, F. Zhang, Y. Shi, L. Cheng, D. Feng, Z. Wu, Z. Chen, Y. Wan, A. Stein and D. Zhao, *Chem. Mater.*, 2006, **18**, 4447-4464.
13 S. Jun, S. H. Joo, R. Ryoo, M. Kruk, M. Jaroniec, Z. Liu, T. Ohsuna and O. Terasaki, *J. Am. Chem. Soc.*, 2000, **122**, 10712-10713.
14 W. Chen, S. Li, C. Chen and L. Yan, *Adv. Mater.*, 2011, **23**, 5679-5683.
15 H. Sun, Z. Xu and C. Gao, *Adv. Mater.*, 2013, **25**, 2554-2560.
16 Y. Wang, X. Wang and M. Antonietti, *Angew. Chem.*, *Int. Ed*., 2012, **51**, 68-89.
17 Y. Wang, J. Zhang, X. Wang, M. Antonietti and H. Li, *Angew. Chem.*, *Int. Ed*., 2010, **49**, 3356-3359.
18 Y. Wang, H. Li, J. Yao, X. Wang and M. Antonietti, *Chem. Sci.*, 2011, **2**, 446-450.
19 X. Zhang, X. Xie, H. Wang, J. Zhang, B. Pan and Y. Xie, *J. Am. Chem. Soc.*, 2013, **135**, 18-21.
20 X. Zhang, H. Wang, H. Wang, Q. Zhang, J. Xie, Y. Tian, J. Wang and Y. Xie, *Adv. Mater.*, 2014, **26**, 4438-4443.
21 T. Ma, Y. Tang, S. Dai, S. Qiao, *Small*, 2014, **10**, 2382-2389.
22 J. Zhang, M. Zhang, L. Lin and X. Wang, *Angew. Chem.*, *Int. Ed*., 2015, **54**, 6297-6301.
23 22. J. Xu, L. Zhang, R. Shi and Y. Zhu, *J. Mater. Chem. A*, 2013, **1**, 14766.
24 J. Zhang, X. Chen, K. Takanabe, K. Maeda, K. Domen, J. D. Epping, X. Fu, M. Antonietti and X. Wang, *Angew. Chem.*, *Int. Ed*., 2010, **49**, 441-444.
25 F. Su, S. C. Mathew, L. Mohlmann, M. Antonietti, X. Wang and S. Blechert, *Angew. Chem.*, *Int. Ed*., 2011, **50**, 657-660.
26 X. Wang, K. Maeda, A. Thomas, K. Takanabe, G. Xin, J. M. Carlsson, K. Domen and M. Antonitti. *Nat. Mater.*, 2009, **8**, 76-80.
27 J. Liu, Y. Liu, N. Liu, X. Zhang, H. Huang, Y. Lifshitz, S. T. Lee, J, Zhong and Z. Kang, *Science*, 2015, **347**, 970-974.
28 P. Niu, L. Zhang, G. Liu and H.-M. Cheng, *Adv. Funct. Mater.*, 2012, **22**, 4763-4770.
29 S. Yang, Y. Gong, J. Zhang, L. Zhan, L. Ma, Z. Fang, R. Vajtai, X. Wang and P. M. Ajayan, *Adv. Mater.*, 2013, **25**, 2452-2456.
30 X. Du, G. Zou, Z. Wang and X. Wang, *Nanoscale*, 2015, **7**, 8701-8706.
31 H. Jiu, W. Jia, L. Zhang, C. Huang, H. Jiao and J. Chang, *J. Porous Mater.*, 2015, DOI: 10.1007/s10934-015-0033-7.
32 R. C. Dante, P. Martín-Ramos, A. Correa-Guimaraes and J. Martín-Gil, *Mater. Chem. Phys.*, 2011, **130**, 1094-1102.
33 J. Xu, H. T. Wu, X. Wang, B. Xue, Y. X. Li and Y. Cao, *Phys. Chem. Chem. Phys.*, 2013, **15**, 4510-4517.
34 M. Sadhukhan and S. Barman, *J. Mater. Chem. A*, 2013, **1**, 2752.
35 A. Vinu, *Adv. Funct. Mater.*, 2008, **18**, 816-827.
36 Y. Li, J. Zhang, Q. Wang, Y. Jin, D. Huang, Q. Cui and G. Zou, *J. Phys. Chem. B*, 2010, **114**, 9429-9434.
37 Y. Cui, J. Zhang, G. Zhang, J. Huang, P. Liu, M. Antonietti and X. Wang, *J. Mater. Chem.*, 2011, **21**, 13032.
38 X. Wang, X. Chen, A. Thomas, X. Fu and M. Antonietti, *Adv. Mater.*, 2009, **21**, 1609-1612.

Graphic Abstract

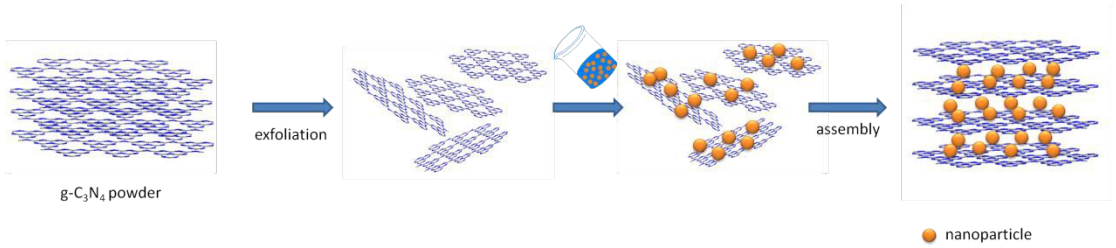

Graphitic carbon nitride based mesoporous materials were constructed via a novel "pillared" way, which can expand the "tool box" available to synthesize multi-functional porous materials.